



HAL
open science

CCE-Net: A rib fracture diagnosis network based on contralateral, contextual, and edge enhanced modules

Y. Gao, H. Liu, L. Jiang, C. Yang, X. Yin, Jean-Louis Coatrieux, Y. Chen

► To cite this version:

Y. Gao, H. Liu, L. Jiang, C. Yang, X. Yin, et al.. CCE-Net: A rib fracture diagnosis network based on contralateral, contextual, and edge enhanced modules. *Biomedical Signal Processing and Control*, 2022, 75, pp.103620. 10.1016/j.bspc.2022.103620 . hal-03634166

HAL Id: hal-03634166

<https://hal.science/hal-03634166>

Submitted on 27 Apr 2022

HAL is a multi-disciplinary open access archive for the deposit and dissemination of scientific research documents, whether they are published or not. The documents may come from teaching and research institutions in France or abroad, or from public or private research centers.

L'archive ouverte pluridisciplinaire **HAL**, est destinée au dépôt et à la diffusion de documents scientifiques de niveau recherche, publiés ou non, émanant des établissements d'enseignement et de recherche français ou étrangers, des laboratoires publics ou privés.



Distributed under a Creative Commons Attribution - NonCommercial 4.0 International License

CCE-Net: A rib fracture diagnosis network based on contralateral, contextual, and edge enhanced modules

Yuan Gao^{1,2}, Hongzhi Liu^{1,2}, Liang Jiang^{3*}, Chunfeng Yang^{1,2}, Xindao Yin³, Jean-Louis Coatrieux⁴, Yang Chen^{1,2*}

1 Laboratory of Image Science and Technology, School of Computer Science and Engineering, Southeast University, Nanjing 210096, China

2 Jiangsu Provincial Joint International Research Laboratory of Medical Information Processing, School of Computer Science and Engineering, Southeast University, Nanjing, 210096, China

3 Department of Radiology, Nanjing First Hospital, Nanjing Medical University, Nanjing 210006, China

4 Centre de Recherche en Information Biomédicale Sino-Francais, Inserm, University of Rennes 1, Rennes 35042, France

First author Yuan Gao's email address: yuangao@seu.edu.cn

Co-first author Hongzhi Liu's email address: liuhongzhi@seu.edu.cn

Corresponding author Yang Chen's email address: chenyang.list@seu.edu.cn

Co-corresponding author Liang Jiang's email address: Jiangliang0402@163.com

ABSTRACT

Rib fracture is a common disease that requires prompt treatment. This study focuses on developing a rib fracture diagnosis deep learning method using contralateral, contextual, and edge enhanced modules and evaluating its detection performance. A novel rib fracture diagnosis method was designed, named CCE-Net. To evaluate the performance of this method, 1639 digital radiography (DR) images were enrolled. Fracture features were extracted for three modules: contralateral, contextual, and edge enhanced modules. These modules can be used to identify fracture features in rib DR images, imitating the experience of broad-certificated radiologists. The contralateral module assists in diagnosing rib fractures by comparing the difference between the detected target region and the contralateral region. The contextual module helps to aid rib fracture detection by extracting contextual features. The edge enhanced module improves the accuracy of fracture detection by enhancing the edge information of the rib bone. The head of this two-stage detection network uses the multi-path fusion mechanism as the main architecture to integrate and utilize the above modules. The qualitative results show that with the ground truth of rib fracture as the evaluation standard, CCE-Net can achieve a better visual effect of fracture detection than other methods. The quantitative results show that CCE-Net can achieve the best performance in various detection indicators include AP50 0.911, AP75 0.794, AP25 0.913, and Recall 0.934. Experimental results show that CCE-Net can acquire the excellent ability of rib fracture diagnosis. We invasion that this approach will be applied to clinical study.

42 *Keywords:* rib fracture, deep learning, contralateral module, contextual module, edge
43 enhanced module

44

45 **1. Introduction**

46 Rib fractures are the most common injury in blunt chest trauma [1–4]. It can cause
47 chest pain and restrict physical mobility [5-11]. People over 45 years old with more
48 than four rib fractures are considered dangerous [12,13]. Rib fractures need to be
49 diagnosed and treated as soon as possible [14,15,16]. There are many reasons why it is
50 necessary to diagnosis rib fractures: it will easily cause respiratory complications such
51 as posttraumatic pneumonia if the diagnosis of rib fractures is not timely [4,17,18]; they
52 are indicators of trauma-related diseases that require immediate treatment, such as
53 pneumothorax and their onset can be delayed for several days [19]; the diagnosis of rib
54 fractures can be used as the basis for further comprehensive treatment strategies [20,21].
55 DR is usually the preferred method of rib fracture detection [22]. Due to the different
56 shapes of rib fractures, the rate of missed diagnosis and misdiagnosis is relatively high
57 [23,24]. Rib fractures can become a life-threatening disease unless detected and treated
58 appropriately, especially in elderly patients [25,26,27]. With the rapid development of
59 artificial intelligence, it is worth introducing deep learning technology to improve rib
60 fracture diagnosis and recognition accuracy as much as possible.

61 Previous work mainly focused on rib fracture detection in CT images. Weikert et
62 al. [28] proposed a deep learning-based prototype algorithm detecting rib fractures on
63 trauma CT on a pre-examination level. Zhou et al. [29] built a CNN model combining
64 CT images and clinical information to detect and classify rib fractures automatically.
65 Urbaneja et al. [30] proposed that CT with unfolded cylindrical projection can be used
66 for rib fracture detection and characterization. Jin et al. [31] used a 3D-UNet model to
67 solve the segmentation problem of rib fractures. Meng et al. [32] helped radiologists
68 achieve high performance in diagnosing and classifying rib fractures on CT images with
69 the assistance of deep learning algorithms. Although the above-mentioned CT-based
70 methods have achieved good performance, there are few excellent methods based on
71 DR. Compared with CT, DR has a faster imaging speed and a smaller radiation dose.
72 DR is the first choice for the radiologist to diagnose rib fractures. Lindsey et al. [33]
73 train a deep learning model to detect fractures on radiographs with a diagnostic
74 accuracy similar to senior subspecialized orthopedic surgeons. Yahalomi et al. [34] train
75 a Faster R-CNN, a machine vision neural network for object detection, to identify and
76 locate distal radius fractures in anteroposterior X-ray images. Thian et al. [35]
77 demonstrate the ability of an object detection CNN to detect and localize radius and
78 ulna fractures on wrist radiographs with high sensitivity and specificity. Kim et al. [36]
79 identify the extent to which transfer learning from deep convolutional neural networks
80 (CNNs), pre-trained on non-medical images, can be used for automated fracture
81 detection on plain radiographs. Kitamura et al. [37] use a convolutional neural network
82 ensemble implemented with a small sample, de novo training, and multiview
83 incorporation to detect ankle fracture. Although there are many deep learning-based
84 fracture detection studies on DR, there are scant clinically reliable rib fracture detection

85 algorithms. Due to low texture contrast, large differences in patient anatomy, and
86 overlapping organs, it is very challenging to detect and locate rib fractures in DR images
87 automatically.

88 This paper proposes a contralateral, contextual, and edge enhanced network (CCE-
89 Net) address the above challenges of detecting rib fractures. CCE-Net mainly adopts a
90 region-based two-stage detector. It combines three novel feature extraction streams: the
91 contralateral module, contextual module, and edge enhancement module, so that
92 accurate feature extraction. Since the left and right parts of the human chest ribs have
93 many similar skeleton structures, radiologists often use the left-right comparison
94 method to help them diagnose rib fractures. To extract the similarity information of the
95 contralateral ribs, the spine line is used as the axis of symmetry to obtain a symmetrical
96 rib patch. The contralateral patch is used as one of the neural network inputs. A fusion
97 module is designed to integrate the features of the disease proposal and its contralateral
98 reference patch. The above experience also applies to the upper and lower ribs, which
99 have structural similarities. The contextual module is integrated into the pipeline. The
100 flatness and smoothness of the bone edges are an important basis for fracture judgment
101 when radiologists diagnose rib fractures. To capture bone edge information, the edges
102 containing the key texture structure of the ribs are extracted. Specifically, the edge
103 information reflecting the bone texture structure is integrated as one of the neural
104 network inputs. Therefore, the above methods can help CCE-Net obtain rich
105 characteristic information and excellent performance. The contributions of the study
106 can be listed as follows.

107 1. This study aimed to develop a novel deep learning-based model for rib fractures
108 automatically detection. The performance of our model is compared with other models
109 in rib fractures detection.

110 2. A two-stage detection method is creatively proposed that can effectively
111 integrate multiple feature extraction modules of the contralateral, contextual, edge
112 enhanced, which makes full use of the unique feature information of the rib image.
113 These modules are similar to the experience of radiologists in diagnosing rib fractures.

114 3. A weight distribution fusion method aims to fuse different image detail features
115 and texture structure features of rib fractures at the decision level. It helps obtain a
116 complete feature representation and enables the model to be trained end-to-end.

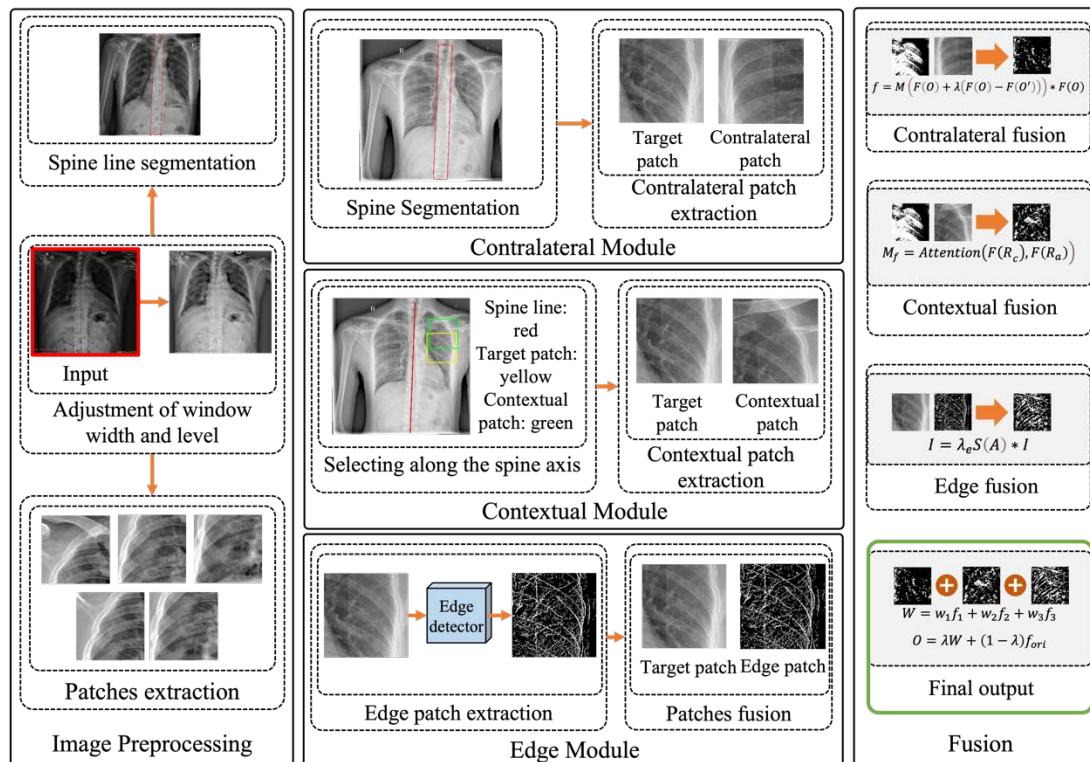
117

118 **2. Material and Methods**

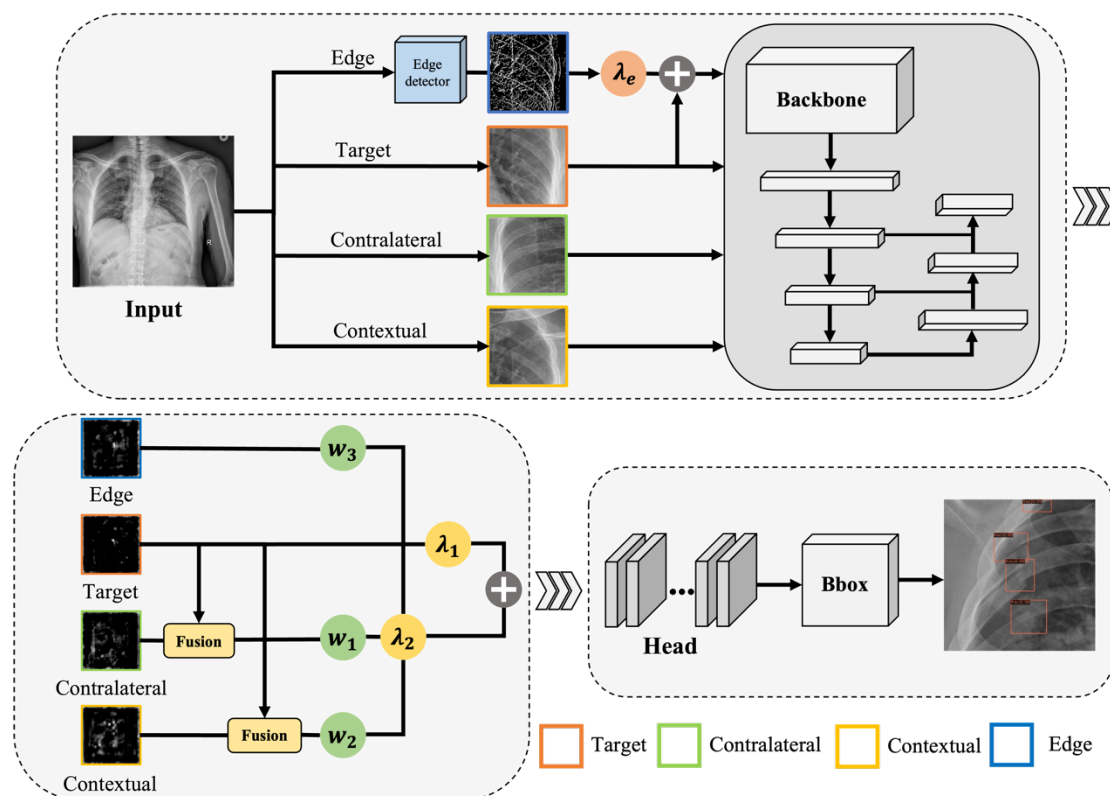
119 **2.1. Network architecture overview**

120 This paper aims to detect rib fractures in DR images automatically. The flow chart
121 for these steps is shown in Fig.1. The radiologists often focus on the differences in
122 different regions and the smoothness of the bone edge as the diagnosis basis of rib
123 fractures. Based on these essentials, the CCE-Net is proposed to exploit contralateral,
124 contextual, and edge texture information to enhance the feature representations of rib
125 fractures. The network architecture of CCE-Net is depicted in Fig.2. The contralateral
126 and contextual patches are extracted according to the spine line segmentation algorithm.
127 The edge images are acquired based on the edge extraction algorithm. These three

128 modules will be used as the neural network inputs to help the two-stage detector achieve
 129 better feature representation. The details are illustrated below.
 130



131
 132 **Fig.1** The workflow of this study. Image preprocessing can extract image patches and
 133 the spine line from original images. Three novel modules (contralateral, contextual,
 134 and edge enhanced) can obtain more features of rib fractures. The feature fusion of the
 135 three modules can assist the basic detection network in achieving performance
 136 improvement. It should be noted that the DR image with the red outline on the left is
 137 used as the input of this method, and the fusion result of the green outline on the right
 138 is used as the output of this method.
 139



140

141 **Fig.2.** The network architecture of CCE-Net. Our proposed method is based on the
 142 two-stage network. It extracts valid information on rib fractures, integrating four
 143 branches marked in orange, green, yellow and blue: target, contralateral, contextual,
 144 and edge. Four branches perform the same feature extraction on the backbone
 145 network. The results of four branches can be effectively fused in the neck stage to
 146 provide more reliable feature information in the subsequent stages.

147

148 2.2. Contralateral module

149 The contrast of the contralateral patch is useful for radiologists to reference.
 150 Especially when fractures are contained in images, the contralateral information helps
 151 differentiate the abnormal and the normal ribs and better highlights the difference of
 152 fracture regions. Considering that the ribs of the human body are symmetrical, and the
 153 spine is situated in the relatively middle position of the chest. The symmetrical central
 154 axis of the ribs on both sides is the same as the line of the human spine. We first roughly
 155 segment the spine line and extract the contralateral patch based on the left-right
 156 symmetry of the ribs.

157

158 2.2.1 Spine line roughly extraction

159 Examining symmetrical regions on both sides of the spine can help radiologists
 160 determine rib fractures. The human spine is a skeletal organ usually located in the center
 161 and has a regular shape in the DR image. Therefore, the spine line is only needed to
 162 roughly segment to examine the contralateral patch of the rib.

163 Specifically, the spine line can be roughly segmented by a CNN model. The UNet
 164 [38] is selected as the spine line segmentation model. We label the spine region on the

165 DR data set and use this data set to train the model. Because the symmetrical central
 166 axis of the ribs on both sides is not a precise line, there is no need for high segmentation
 167 accuracy requirements for the spine segmentation model.

168 The minimum circumscribed quadrilateral enclosing the spine mask can be obtained.
 169 The spine line bridged by the centers of two short edges is regarded as the symmetric
 170 axis. The spine line can be expressed as $Ax + By + C = 0$. The target patch is denoted
 171 as $P_{target}(x_a, y_a)$, and the contralateral patch can be denoted as $P_{contra}(x_b, y_b)$. The
 172 following formula can express the contralateral patch:

$$\begin{aligned} x_b &= \frac{x_a - (2A * (Ax_a + By_a + C))}{A^2 + B^2} \\ y_b &= \frac{y_a - (2B * (Ax_a + By_a + C))}{A^2 + B^2} \end{aligned} \quad \text{Eq (1)}$$

173 After the central axis of symmetry is determined, the region symmetrical with the
 174 target region according to the spine symmetry axis can be determined as the
 175 contralateral patch.

176

177 2.2.2. Contralateral images fusion

178 After obtaining the contralateral patch, the characteristics of the highly similar
 179 structure on both sides of the human ribs are used to pair each target patch with its
 180 contralateral patch. An attention mechanism uses the difference between the target and
 181 contralateral patch in high-level semantic features to guide the potential location of the
 182 fracture. The contrast-induced attention [39] is used to fuse features of each target patch
 183 and its contralateral patch.

184 The feature fusion process of the target area and the opposite patch feature is shown
 185 in Fig.3. We define the target patch as O , and the contralateral patch obtained as O' .
 186 They perform the same convolution operation as F in the backbone network. The
 187 feature maps are effectively fused to realize the contralateral information extraction.
 188 The fusion operation adopts a pixel-by-pixel method. The subtraction operation
 189 between $F(O)$ and $F(O')$ helps provide contrast information and suppress the response
 190 of attributes unrelated to fracture recognition and location. On the other hand, adding
 191 the above subtraction results from the target patch is helpful to identify the same
 192 structural information of the ribs with larger responses in the patches on both sides. The
 193 attention module M encodes $F(O)$ and $F(O')$ into the attention maps. The attention
 194 maps are multiplied pixel by pixel to weight the original target feature map to obtain f .
 195 The operation is shown below.

$$f = M \left(F(O) + \lambda(F(O) - F(O')) \right) * F(O) \quad \text{Eq (2)}$$

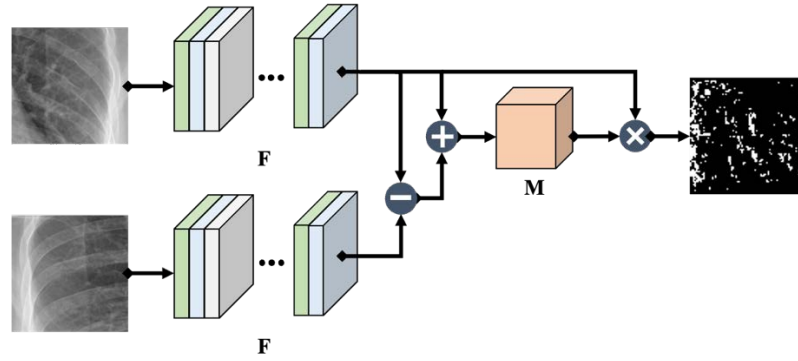


Fig.3. An overview of the fusion flow. It aims to fuse the effective information of each part to extract the results. The addition and subtraction of the contralateral patch and the target patch are effectively fused with the target patch by using the attention module.

2.3. Contextual module

Focusing on multiple adjacent ribs can make the detection more accurate. The normal rib is similar in shape and signal intensity to its adjacent normal rib. By checking on the contextual information of the diagnosed region, the radiologists can intuitively obtain the changes in the appearance of bones due to fractures. A contextual module that takes adjacent contextual ribs as input is designed to imitate a radiologist.

2.3.1. Contextual images extraction

The longitudinal position of each diagnosed rib region needs to be judged according to the rough segmentation result of the spine. Since there are no more than 12 human ribs on each side [40], one of the adjacent upper and lower rib regions should be selected as the input of the context module. If the longitudinal position belongs to the upper region of the spine, the adjacent rib region on the lower side is taken as the input of the context module; otherwise, the adjacent rib region on the upper side is taken as the input of the context module. After the patch direction selection decision is determined, the diagnosed rib patch can be moved along the extension direction of the spine's central axis by half of the boundary length to obtain the context patch. It should be noted that the boundary length refers to the width of the patch, and this study uses 640 pixels as the patch width. Due to the short distance between the adjacent ribs of the human body, half the distance of the moving patch boundary can sufficiently cover the adjacent ribs.

2.3.2. Contextual images fusion

The contextual module is designed to take two adjacent ribs as input patches, including the current diagnosis rib and its adjacent rib. A two-branch structure is used to compare adjacent ribs to identify fractures. This structure uses the same fusion method as in Equation 2 in the previous section. We denote the two patches of the current diagnosis rib and its adjacent rib as R_c and R_a , respectively. These two branches have the same feature extraction network as F . The resulting feature map uses the attention mechanism for feature layer fusion and then is input to the rest of the

convolution of the overall network. The final fusion feature maps M_f can be expressed as:

$$M_f = \text{Attention}(F(R_c) + \lambda(F(R_c) - F(R_a))) \quad \text{Eq (3)}$$

234

235 **2.4. Edge enhanced module**

236 To capture the edge information of the ribs in the image, we extract the edges
 237 containing key texture information for visual recognition and integrate the edge map
 238 with the neural network model to improve fracture detection. Rib fractures are highly
 239 correlated with the appearance of the bone edges of the ribs. For example, a fractured
 240 rib will show abnormal curvature of the skeletal cortex. Based on the above experience,
 241 we believe that purely enforcing the widening of the receptive field is not sufficient for
 242 rib fracture detection, and the introduction of more comprehensive edge information
 243 can improve the detection effect. Since the edges reflect local intensity changes and
 244 display the boundary information of ribs in the image, maintaining the edges can
 245 preserve the structure of the image content and the texture details.

246

247 **2.4.1. Edge enhanced images extraction**

248 The edge information is added to the neural network to enforce the feature map's
 249 integration with the original image's edge information. The Sobel operator can calculate
 250 the edge map due to its simplicity. Sobel filters S are used to convolve the original
 251 image I_o to generate the edge map. Then, the edge information map is integrated into
 252 the input image I by addition pixel by pixel as the following equation:

$$I_e = \lambda_e S(I_o) \oplus I \quad \text{Eq (4)}$$

253 Where λ_e means the scale factor of edge information, and \oplus means the operation of
 254 addition pixel by pixel.

255 By adding the scale factor calculated by the Sobel operator to the input image, the
 256 neural network can integrate the information of texture structure and edge intensity to
 257 pay more attention to the rib edge information and reduce the sensitivity to noise. The
 258 Sobel filter assigns higher weights to the edge region of the original image and lower
 259 weights to other regions, which directly enhances the use of image edges by the neural
 260 network.

261

262 **2.5. Fusion architecture**

263 As shown in Fig.2, all three parts are integrated into the whole framework. Our
 264 work aims to integrate each region proposal feature f of contralateral, contextual and
 265 edge enhanced modules into the final output O . Integrate by simply connecting
 266 operation to make the contribution of each stream equal, which may ignore the high-
 267 value features from a module. Feature fusion methods may enhance some feature
 268 modules and suppress some feature modules. If we simply combine each feature
 269 extraction module mechanically, it is easy to lose the features that should be enhanced.
 270 Therefore, we need to design a fusion method that conforms to the characteristics of
 271 deep learning. This study needs to select appropriate scale features for different feature
 272 extraction modules. The effective fusion of features is achieved by introducing self-
 273 learning to select appropriate scales. We link the results of the three modules by

274 assigning different weight factors to the feature extraction module through the weight
 275 distribution module. A weight distribution module is introduced as W that can perform
 276 backward propagation and adaptively determine the weights of different modules. The
 277 weight distribution module is inspired by the attention mechanism and consists of
 278 multiple convolutional and pooling layers. The specific process can be expressed as the
 279 following Equation 5:

$$W = w_1 f_1 + w_2 f_2 + w_3 f_3 \quad \text{Eq (5)}$$

280 Where f_1 , f_2 and f_3 mean the feature maps result of contralateral, contextual and edge
 281 enhanced modules, w_1 , w_2 and w_3 mean the attention mechanism operation.

282 The final output feature maps of CCE-Net can be expressed as O :

$$O = \lambda W + (1 - \lambda) f_{ori} \quad \text{Eq (6)}$$

283 Where f_{ori} means the feature maps of original rib patch, λ means the parameter
 284 weighting the importance of these three modules.

285

286 **2.6. Loss function**

287 The detection network architecture that combines the above three modules has been
 288 established. The loss function can calculate the error between actual values and
 289 predicted values. Cross entropy loss is chosen as the objection function and is given by
 290 Eq (7):

$$loss = -\frac{1}{N} \sum (y \times \log(\hat{y}_m) + (1 - y) \times \log(1 - \hat{y}_m)) \quad \text{Eq (7)}$$

291 where y is the label and y_m is the predicted output vector.

292

293 **3. Experimentals and Results**

294 **3.1. Dataset**

295 A private dataset named Rib-NJFH is collected to train and validate our proposed
 296 method. Due to the protection of patient privacy, please forgive us that the dataset used
 297 in this study cannot be publicly available. The dataset contains 1639 DR images from
 298 Nanjing First Hospital, among which there are 2703 rib fractures. We use 1311 images
 299 for training, 164 images for validating, and 164 images for testing. All images are
 300 annotated and examined by experienced radiologists.

301

302 **3.2. Evaluation metrics**

303 The bounding box AP [41] and recall are calculated to evaluate the performance of
 304 the model. Considering rib fractures as a general target, AP50 is used as the main
 305 evaluation index. AP25 and AP75 are used as references. We believe that AP75 better
 306 reflects the accurate positioning performance of the fracture region due to its strict
 307 evaluation criteria, AP25 has relatively loose evaluation criteria to determine whether
 308 the test results are misjudged and thus better reflects the recognition performance of rib
 309 abnormalities, AP50 is a comprehensive performance index for fracture recognition and
 310 regional positioning [42, 43].

$$AP = \int_0^1 P(r) dr \quad \text{Eq (9)}$$

311

312 The PR curve with the corresponding AUCs was calculated for validation datasets
 313 to evaluate the performance of the model. The Recall is defined by Eq (10):

$$314 \quad \text{Recall} = \frac{TP}{TP + FN} \quad \text{Eq (10)}$$

314 Where TP and FN are the numbers of positive samples correctly classified and
 315 incorrectly classified, TN and FP are the numbers of negative samples correctly
 316 classified and incorrectly classified.

317

318 **3.3. Implementation details**

319 The segmentation of the spine's central axis is needed to use in the contralateral
 320 module and the contextual module for our experiment. Specifically, the spine regions
 321 of the training set are labeled. An example of spine labeling is shown in Fig.4. The
 322 segmentation algorithm is used to complete the segmentation of the spine region in the
 323 image preprocessing part. After the segmentation results are obtained, image
 324 morphology is used to extract the central axis from the spine mask to obtain the
 325 contralateral patch.

326



327

328 **Fig.4.** The spine line obtention. A red box marks the spine segmentation result. The
 329 spine line is used as the position basis of the image extraction of the contralateral
 330 module and the contextual module.

331

332 The data set is divided into the training set, the validation set and the test set at
 333 8:1:1. The image patches randomly cropped from DR images are resized to 640×640
 334 pixels. Rotation, horizontal and vertical flipping are used for data augmentation. All
 335 experiments are implemented using Pytorch on 2 NVIDIA 1080Ti GPUs. ResNet-50 is
 336 used as the backbone of the proposed method. We train our model for 50 epochs and
 337 test it every five times. For all training, the optimizer is stochastic gradient descent
 338 (SGD) with a weight decay of 0.001 and momentum of 0.9 to optimize all models and
 339 the batch-size is 2 on each GPU. The learning rate starts at 0.01 and reduces by a factor
 340 of 10 after 30 and 40 epochs.

341

342 **3.4. Models comparison**

343 According to the characteristics of our dataset and detection task, we compare with
 344 methods that include Faster RCNN [44], Libra RCNN [45], Dynamic RCNN [46],
 345 Cascade RCNN [47] and YOLO v4 [48].

346

347 **3.4.1. Quantitative Results**

348 To validate the performance of CCE-Net, five mainstream algorithms are selected
 349 to implement the comparison experiments. For rib DR images, the performance metrics
 350 in the training sets can be achieved with the accuracy of 99.648 and the loss of 0.027.
 351 The validation set can achieve AP50 and Recall of 0.910 and 0.938. In the test sets, the
 352 model's detection performance yielded the AP50 of 0.911, and the Recall is 0.934, as
 353 shown in Table 1.

354
 355 Table 1 The quantitative comparisons performance of our method.

Method	AP50	AP75	AP25	Recall	AUC
Faster RCNN	0.787	0.349	0.878	0.875	0.816
Libra RCNN	0.825	0.326	0.862	0.886	0.847
Dynamic RCNN	0.887	0.516	0.904	0.903	0.901
Cascade RCNN	0.910	0.781	0.911	0.929	0.933
YOLO v4	0.813	0.689	0.816	0.881	0.840
CCE-Net	0.911	0.794	0.913	0.934	0.941

356
 357 The five comparison models, including 'Faster RCNN with ResNet-50', 'Libra
 358 RCNN', 'Dynamic RCNN', 'Cascade RCNN with ResNeXt-101' and 'YOLO v4', are
 359 re-implemented using our dataset. We are committed to merging our proposed module
 360 into a two-stage network of Faster RCNN with ResNet-50 as introduced in Section
 361 3. The performance of our method compared with different methods is presented in
 362 Table 1. The experimental results in Table 1 show that our method achieves the best
 363 performance in all evaluation metrics. Our method equipped with 'Faster RCNN'
 364 achieves 15.76% AP50, 127.5% AP75 and 3.99% AP75 higher than the results of the
 365 original 'Faster RCNN' respectively, the Recall increase by 6.74%, which shows the
 366 advantages of the network in the rib fracture detection ability. In addition, due to the
 367 ResNet-50 backbone network, our method can achieve fast detection speed while
 368 ensuring detection accuracy.

369 For all indicators, our method can achieve better results than other methods. The
 370 improvement of AP50 brought by our method is 10.42% (from 0.825 to 0.911), 2.71%
 371 (from 0.887 to 0.911) and 1.1% (from 0.91 to 0.911) when using 'Libra RCNN',
 372 'Dynamic RCNN' and 'Cascade RCNN with ResNeXt-101' to produce rib fracture
 373 proposals. Compared with 'YOLO v4', which is the one-stage model and achieved
 374 outstanding detection performance, the one-stage model with 'YOLO v4' achieves
 375 0.813 AP50 and 0.881 Recall. Our method is 0.098 and 0.053 higher than the 'YOLO
 376 v4' results, respectively.

377

378 **3.4.2. Qualitative Results**

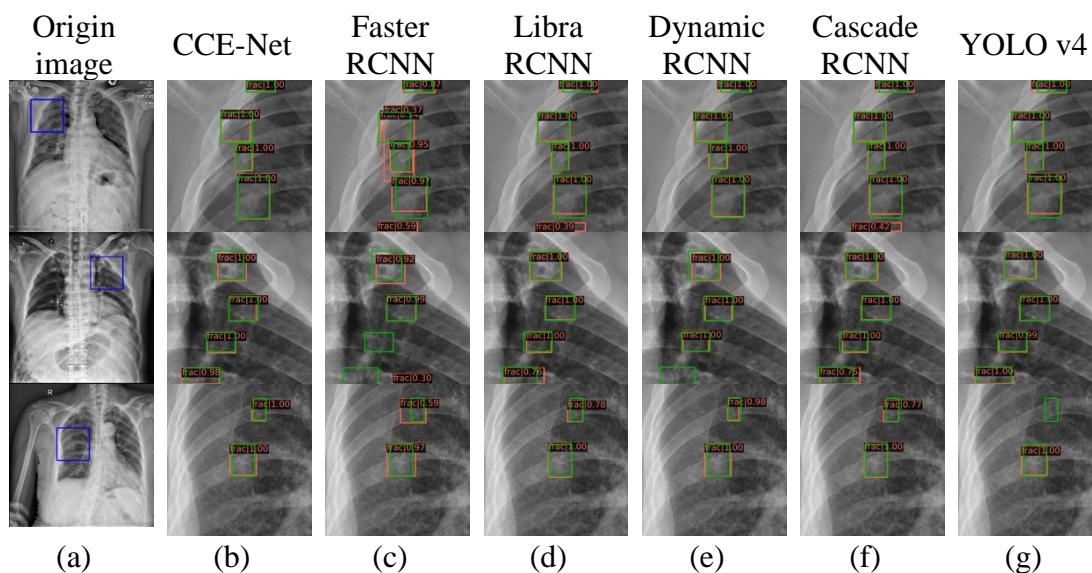
379 Visualization images are used to show the difference between the proposed method
 380 and other methods. The results of CCE-Net and other methods are shown in Fig.5. The
 381 second column is the result of the proposed method. CCE-Net can effectively detect
 382 fracture targets. The third to seventh columns are the results of comparison methods.
 383 There are missed detections and false detections in the results of comparison methods.

384 To illustrate the effectiveness of information extraction, feature maps of three
 385 different layers are visualized. The visualization includes the result and the feature maps

386 with sizes of 64, 32, 16 pixels. The feature maps of different sizes are enlarged to the
 387 same size and displayed by superimposing the original image. As shown in Fig.6, the
 388 proposed method can focus on more reasonable regions. Overall, the correctness of the
 389 proposed method is the best because it focuses on more reasonable image features.

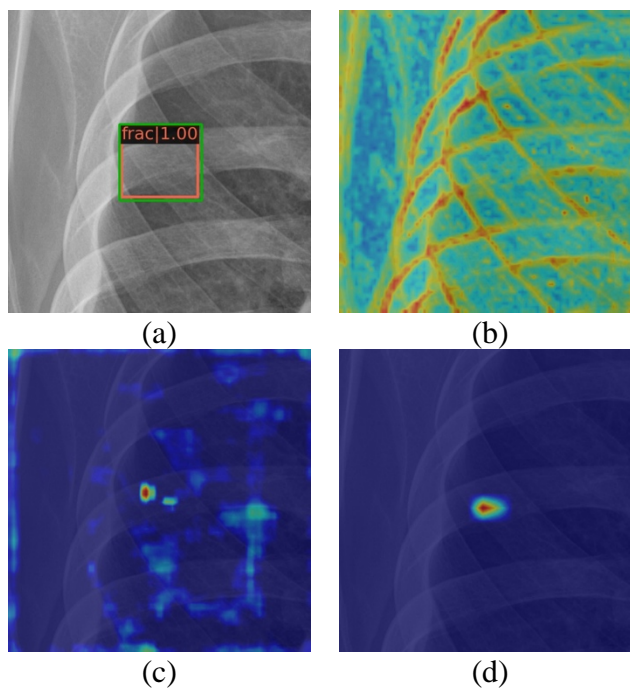
390 The PR curves of different methods on the validation data can be shown in Fig.7.
 391 For the results of CCE-Net with rib fractures detection, the method obtains good
 392 performance.

393

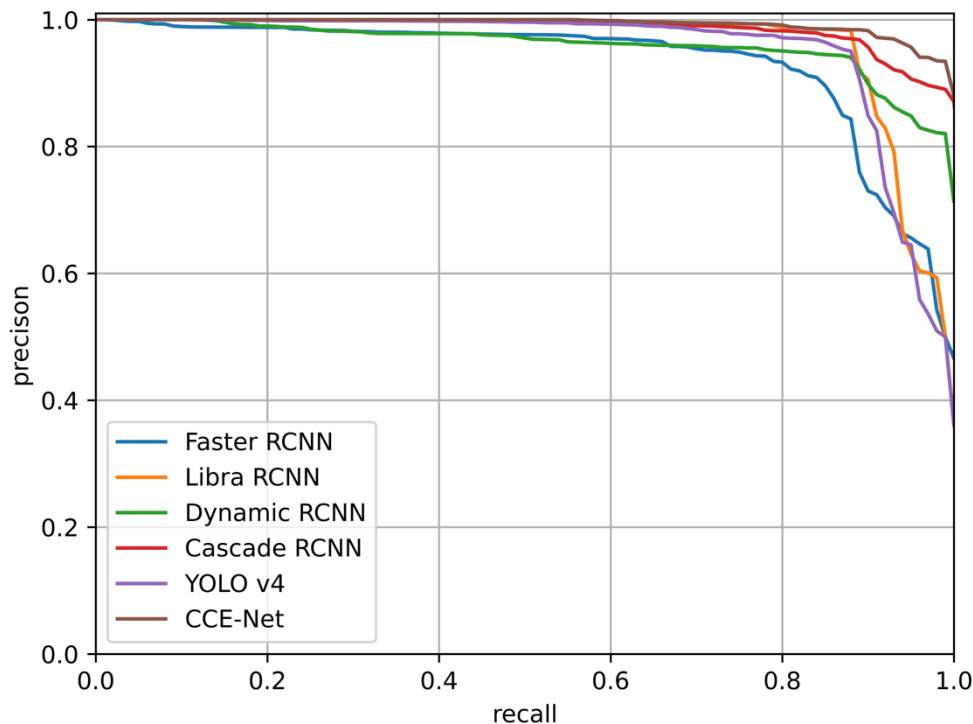


394 **Fig.5.** The results demonstrate that the CCE-Net with three modules has better
 395 detection Precision and Recall performance. Blue, green, and red boxes stand for the
 396 patch position, ground truth, and results, respectively. (a) represent origin images. (b),
 397 (c), (d), (e), (f), and (g) represent results obtained via CCE-Net, Faster RCNN, Libra
 398 RCNN, Dynamic RCNN, Cascade RCNN, and YOLO v4, respectively.

399



400 **Fig.6.** The visualization images show that the CCE-Net can pay more attention to the
 401 rib fracture region as the decline in feature maps size. Feature maps are superimposed
 402 displayed on the original image through uniform scaling. (a) represent the result. (b),
 403 (c), and (d) represent the feature map of different sizes of 64*64, 32*32, and 16*16,
 404 respectively.
 405



406 **Fig.7.** The PR curves show that the CCE-Net has the best performance compared
 407 with other methods.
 408

409

410 3.5. Ablation study

411 To validate the effectiveness of each module, an ablation study is conducted on the
 412 proposed model. We use the same training, validation, and test sets in all experiments.
 413 The ‘Faster RCNN with ResNet-50’ is used as the baseline model. The contralateral,
 414 contextual, and edge enhanced modules are removed from CCE-Net. The results of
 415 ablation are shown in Table 2 and Fig.8. The PR curves of the ablation experiment can
 416 be seen in Fig.9, which demonstrates the enhancement of our method.
 417

417

418 3.5.1. The effect of contralateral module

419 Compared with CCE-Net, if we remove the contralateral module, the performance
 420 is decreased by 1.9% and 0.76% on AP50 and Recall, respectively. The decline on AP50
 421 validates the effectiveness of the contralateral module on overlapping positions.
 422

422

423 3.5.2. The effect of contextual module

424 Removing the contextual module decreases performance by 1.67% and 2.52% on
 425 AP50 and Recall, respectively, compared with CCE-Net. It indicates that the contextual
 426 module enhances feature representation more for regions of structure repetition. When

427 adding the contextual module, partial fracture judgment is corrected based on the upper
 428 and lower adjacent ribs.

429

430 3.5.3. The effect of edge enhanced image module

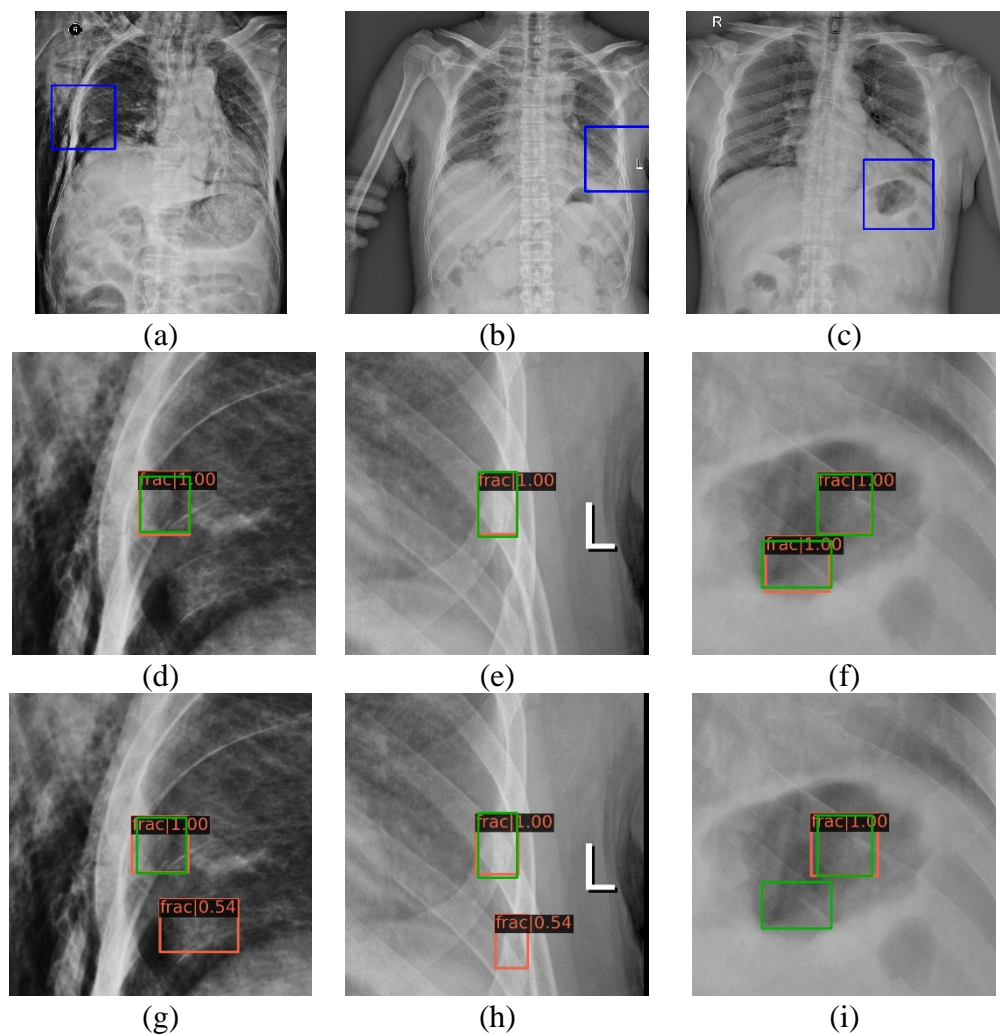
431 Compared with the contralateral module and contextual module, adding the edge
 432 enhanced module can boost the performance by 7.05% and 7.6% on AP50 and Recall,
 433 respectively. The edge enhanced module is encoded by edge information and texture
 434 information. This encoding mechanism affects the rib fracture localization, making the
 435 proposed method obtain more edge information gains.

436

437 Table 2 The ablation study of our method.

	Contralateral module	Contextual module	Edge enhanced module	AP50	Recall	AUC
CCE-Net	*	*	*	0.911	0.934	0.941
	remove	*	*	0.894	0.927	0.933
	*	remove	*	0.896	0.911	0.938
	*	*	remove	0.851	0.868	0.909

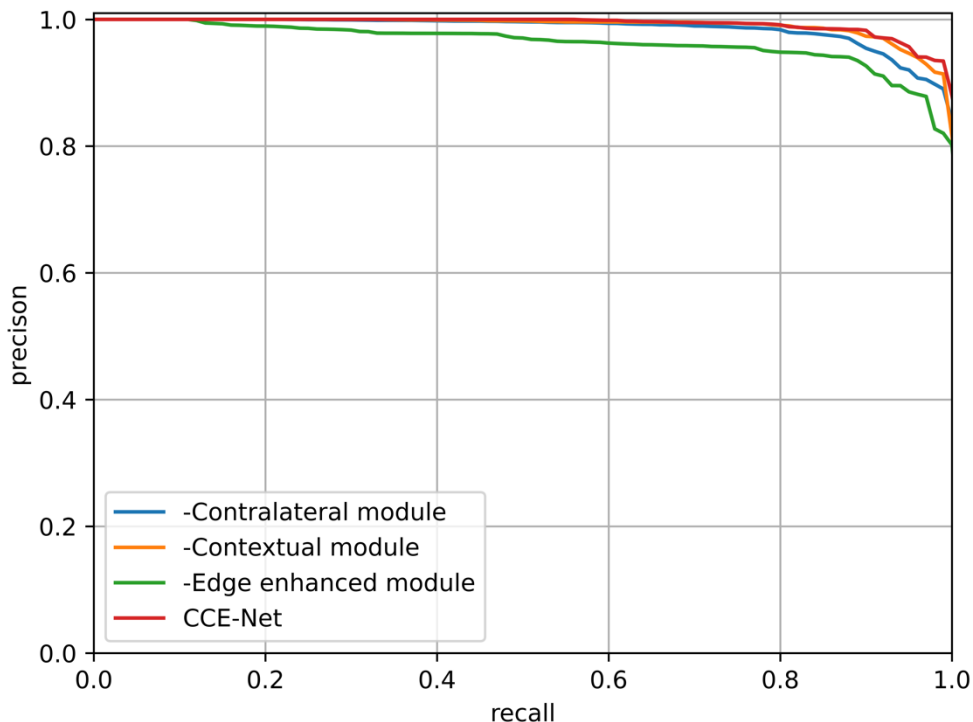
438



439

Fig.8. These comparison cases show that the contralateral, contextual, and edge

440 enhanced module can improve detection capabilities at overlapping positions,
 441 structure repetition regions, and complex edge locations, respectively. (a), (b), and (c)
 442 represent different origin images. (d), (e), and (f) represent CCE-Net. (g), (h), and (i)
 443 represent the results of removing the contralateral module, contextual module, and
 444 edge enhanced module, respectively.
 445



446 **Fig.9.** The PR curves show the comparison of the ablation study.
 447
 448

449 **4. Discussion**

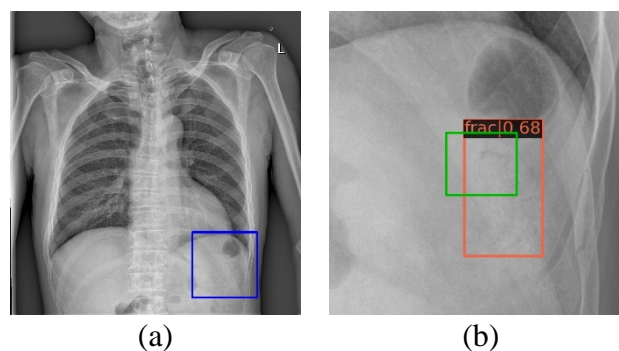
450 This study proposes a novel network architecture for image detection of rib
 451 fractures. Three modules are integrated into the Faster RCNN [44] framework. The
 452 contralateral module is used to obtain contralateral information of the same structure
 453 on both sides of the spine. The contextual module is added to extract image features of
 454 the upper and lower positions of the ribs. The edge enhanced module can stress rib
 455 image edges and obtain the target details more effectively. Experimental results show
 456 that combining these three modules improves the rib fracture detection performance in
 457 evaluation indicators. Compared to the performance of the Faster RCNN, AP50 is
 458 observed to increase by 15.76% from 0.787 to 0.911 and Recall increases by 6.74%
 459 from 0.875 to 0.934. Even compared with many mainstream detection algorithms,
 460 including Faster RCNN [44], Libra RCNN [45], Dynamic RCNN [46], Cascade RCNN
 461 [47] and YOLO v4 [48] in our experiment, the proposed method exhibits a certain
 462 performance improvement in detection effect and fewer training parameters. The
 463 ablation experiments are also conducted on CCE-Net by removing different modules.
 464 The methods after removing different modules have a certain degree attenuation of the
 465 detection effect in different scenarios. It is verified that the proposed method can detect

466 various rib fracture features more effectively and comprehensively.

467 Rib image data are more conducive to detecting fractures when combined with the
 468 visual features of contralateral, contextual and edge images. One elaborate fusion way
 469 to accomplish the features fusion process is to fuse image features from three modules
 470 at different network stages. The feature fusion process at the neck of basic two-stage
 471 network architecture is designed for the contralateral and contextual modules. They
 472 have different original images requiring feature extraction at the backbone stage. The
 473 edge image is added to the rib image straightforwardly before feature extraction for the
 474 edge enhanced module. In the feature fusion process details, we innovatively used a
 475 mixture of numerical operations and attention mechanisms to achieve a better feature
 476 fusion strategy. Besides, the different information contained in the three modules is
 477 needed to combine to make the final decision. The reasonable weight control of each
 478 feature channel is designed at the neck stage of the network, expecting that the proposed
 479 method can simulate the clinical diagnosis ideas of radiologists.

480 Although the proposed network architecture has good detection capabilities in rib
 481 fracture images, the detection results still have several limitations due to the complexity
 482 of medical data. Some failure cases are shown in Fig.10. The limitations of our method
 483 are as follows: (1) For some DR images, due to the curvature of the spine, the accurate
 484 extraction of curved spine lines still needs to solve; (2) Whether the texture and
 485 structural similarity of rib images can be better integrated is also an interesting research
 486 topic. To settle these issues, it deserves further study to design a more efficient module
 487 to explore the contralateral contextual information and enhance the extraction of
 488 information.

489



490 **Fig.10.** These failure cases demonstrate that our proposed method is still worth
 491 improving. (a) The origin image, (b) CCE-Net.

492

493 5. Conclusion

494 This study proposed a CCE-Net based on contralateral, contextual, and edge
 495 enhanced modules to detect rib fracture. A rib fracture is a kind of small target object,
 496 which is difficult to detect integrally. Following the valuable experience of radiologists
 497 in diagnosis, new modules were added to the design of the detection network. CCE-Net
 498 unified contralateral, contextual and edge information together. Compared with the
 499 traditional detection network, CCE-Net can capture more effective information. We
 500 established the rib fracture database with 1639 DR rib images to train the CCE-Net

501 model. A total of 2703 rib fractures were in our database labeled by experienced
502 radiologists. Based on experiments, compared with other methods, its performance can
503 improve the medical image detection ability of rib fracture targets. The detection
504 performance of the CCE-Net was significantly improved than the current methods.
505 CCE-Net attained AP50 0.911, AP75 0.794, AP25 0.913, and Recall 0.934. It can
506 reduce workload for radiologists and assist radiologists in rib fracture diagnosis.

507

508 **Acknowledgments**

509 This work was supported in part by the Postgraduate Research & Practice
510 Innovation Program of Jiangsu Province under Grants SJCX21_0635; in part by the
511 Xinghuo Talent Program of Nanjing First Hospital; in part by the State's Key Project
512 of Research and Development Plan under Grants 2017YFA0104302,
513 2017YFC0109202, and 2017YFC0107900, in part by National Natural Science
514 Foundation under Grants 81530060 and 61871117, in part by the Science and
515 Technology Program of Guangdong under Grant 2018B030333001.

516

517 **CRedit authorship contribution statement**

518 Yuan Gao: Conceptualization, Methodology, Formal analysis, Data curation, Validation,
519 Writing. Hongzhi Liu: Conceptualization, Methodology, Writing, Validation,
520 Investigation. Yang Chen: Funding acquisition, Writing, Validation, Investigation.
521 Liang Jiang: Funding acquisition, Conceptualization, Methodology, Supervision,
522 Writing. Chunfeng Yang: Data curation, Writing. Xindao Yin: Formal analysis, Data
523 curation, Funding acquisition, Supervision. Jean-Louis Coatrieux: Data curation,
524 Writing.

525

526 **Conflict of Interest**

527 The authors declare that they have no known competing financial interests or
528 personal relationships that could have appeared to influence the work reported in this
529 paper.

530

531 **Reference**

- 532 1. S.H. Cho, Y.M. Sung, M.S. Kim, Missed rib fractures on evaluation of initial
533 chest CT for trauma patients: Pattern analysis and diagnostic value of coronal
534 multiplanar reconstruction images with multidetector row CT, *Br J Radiol.* 85
535 (2012) 845-850.
- 536 2. M.P. Fredric, M. Sarah, A.O. Francis, A. Darwin, D. Andrew, G.E. John, F.
537 Bruce, G. Mario, M. Silvana, M. Christian, S. Babak, T. William, H. V. Don,
538 W.W. Thomas, Consensus statement: surgical stabilization of rib fractures rib
539 fracture colloquium clinical practice guidelines, *Injury.* 48 (2017) 307-321.
- 540 3. J.C. Mayberry, D.D. Trunkey, The fractured rib in chest wall trauma, *Chest Surg*

- 541 Clin N Am. 7 (1997) 239-261.
- 542 4. B.S. Talbot, C.P. Gange, A. Chaturvedi, N. Klionsky, S.K. Hobbs, A. Chaturvedi,
543 Traumatic rib injury: Patterns, imaging pitfalls, complications, and treatment,
544 Radiographics. 37 (2017) 628-651.
- 545 5. F.C. Lin, R. Li, Y. Tung, K. Jeng, S.C. Tsai, Morbidity, mortality, associated
546 injuries, and management of traumatic rib fractures, J Chinese Med Assoc. (2016)
547 6-11.
- 548 6. B. Eric, L. Andre, C. David, M. Lynne, R. Sebastien, T. Stephane, L. Jacques,
549 M. Marcel, Elderly trauma patients with rib fractures are at greater risk of death
550 and pneumonia, Journal of Trauma and Acute Care Surgery. 54 (2003) 478-485.
- 551 7. S. RobTodd, M.M. McNally, J.B. Holcomb, R. A. Kozar, L.S. Kao, E.A.
552 Gonzalez, C.S. Cocanour, G.A.Vercruyse, M.H. Lygas, B. K. Brasseaux, F.A.
553 Moore, A multidisciplinary clinical pathway decreases rib fracture-associated
554 infectious morbidity and mortality in high-risk trauma patients, The American
555 Journal of Surgery. 192 (2006) 806-811.
- 556 8. R.M. Shorr, A. Rodriguez, M.C. Indeck, M.D. Crittenden, S. Hartunian, R.A.
557 Cowley, Blunt chest trauma in the elderly, The Journal of Trauma. 29 (1989)
558 234-237.
- 559 9. F. Birse, H. Williams, D. Shipway, E. Carlton, Blunt chest trauma in the elderly:
560 an expert practice review, Emergency Medicine Journal. 37 (2020) 73-78.
- 561 10. D. Stephanie, A. Affatato, Blunt chest trauma: utility of radiological evaluation
562 and effect on treatment patterns, The American journal of emergency medicine.
563 26 (2006) 482-486.
- 564 11. L. Fabricant, B. Ham, R. Mullins, J. Mayberry, Prolonged pain and disability are
565 common after rib fractures, The American Journal of Surgery. 205 (2013) 511-
566 516.
- 567 12. J.B. Holcomb, N.R. McMullin, R.A. Kozar, M.H. Lygas, F.A. Moore, Morbidity
568 from rib fractures increases after age 45, Journal of the American College of
569 Surgeons. 196 (2003) 549-555.
- 570 13. B.T. Flagel, F.A. Luchette, R.L. Reed, T.J. Esposito, K.A. Davis, J.M.
571 Santaniello, R.L. Gamelli, Half-a-dozen ribs: The breakpoint for mortality,
572 Surgery. 138 (2005) 717-725.
- 573 14. R. Kent, W. Woods, O. Bostrom, Fatality risk and the presence of rib fractures,
574 Annals of Advances in Automotive Medicine/Annual Scientific Conference,
575 Association for the Advancement of Automotive Medicine. 52 (2008).
- 576 15. W.M. Wu, Y. Yang, Z.L. Gao, T.C. Zhao, W.W. He, Which is better to multiple
577 rib fractures, surgical treatment or conservative treatment?, International journal
578 of clinical and experimental medicine. 8 (2015) 7930.
- 579 16. M. Sirmali, H. Türüt, S. Topçu, E. Gülhan, Ü. Yazıcı, S. Kaya, I. Taştepe, A
580 comprehensive analysis of traumatic rib fractures: morbidity, mortality and
581 management, European Journal of Cardio-Thoracic Surgery. 24 (2003) 133-138.
- 582 17. S.W. Ho, Y.H. Teng, S.F. Yang, H.W. Yeh, Y.H. Wang, M.C. Chou, C.B. Yeh,
583 Risk of pneumonia in patients with isolated minor rib fractures: a nationwide
584 cohort study, BMJ open. 7 (2017) e013029.

- 585 18. H. Tanaka, T. Yukioka, Y. Yamaguti, S. Shimizu, H. Goto, H. Matsuda, S.
586 Shimazaki, Surgical stabilization of internal pneumatic stabilization? a
587 prospective randomized study of management of severe flail chest patients, *J*
588 *Trauma*. 52 (2002) 727-732.
- 589 19. M.S. Lu, Y.K. Huang, Y.H. Liu, H.P. Liu, C.L. Kao, Delayed pneumothorax
590 complicating minor rib fracture after chest trauma, *Am J Emerg Med*. 26 (2008)
591 551-554.
- 592 20. M. Bemelman, M.W. de Kruijf, B.M. van, L. Leenen, Rib fractures: To fix or
593 not to fix? An evidence-based algorithm, *Korean J Thorac Cardiovasc Surg*. 50
594 (2017) 229-234.
- 595 21. M.B. de Jong, M.C. Kokke, F. Hietbrink, L.P.H. Leenen, Surgical management
596 of rib fractures: Strategies and literature review, *Scand J Surg*. 103 (2014) 120-
597 125.
- 598 22. E.G. Hwang, Y. Lee, Simple X-ray versus ultrasonography examination in blunt
599 chest trauma: effective tools of accurate diagnosis and considerations for rib
600 fractures, *J Exerc Rehabil*. 12 (2016) 637-641.
- 601 23. J. Malghem, B.C. Vande Berg, F.E. Lecouvet, B.E. Maldague, Costal cartilage
602 fractures as revealed on CT and sonography. *Am J Roentgenol*, 176 (2001) 429-
603 432.
- 604 24. M. Kara, E. Dikmen, H.H. Erdal, I. Simsir, S.A. Kara, Disclosure of unnoticed
605 rib fractures with the use of ultrasonography in minor blunt chest trauma, *Eur J*
606 *Cardio-thoracic Surg*. 24 (2003) 608-613.
- 607 25. L.I.G. Worthley, Thoracic epidural in the management of chest trauma, *Intensive*
608 *Care Med*. 11 (1985) 312-315.
- 609 26. Y. Barnea, H. Kashtan, Y. Skornick, N. Werbin, Isolated rib fractures in elderly
610 patients: Mortality and morbidity, *Can J Surg*. 45 (2002) 43-46.
- 611 27. T.J. Ellis, Hip fractures in the elderly, *Curr Womens Health Rep*. 3 (2003) 75-
612 80.
- 613 28. T. Weikert, L.A. Noordtzi, J. Bremerich, S. Bram, P. Victor, C. Joshy, S. Gregor,
614 W.S. Alexander, Assessment of a deep learning algorithm for the detection of
615 rib fractures on whole-body trauma computed tomography, *Korean J Radiol*. 21
616 (2020) 891-899.
- 617 29. Q.Q. Zhou, W. Tang, J. Wang, Z.C. Hu, Z.Y. Xia, Z. Rongguo, X. Fan, W. Yong,
618 X. Yin, B. Zhang, H. Zhang, Automatic detection and classification of rib
619 fractures based on patients' CT images and clinical information via
620 convolutional neural network, *Eur Radiol*. 31 (2021) 3815-3825.
- 621 30. A. Urbaneja, J. De Verbizier, A.S. Formery, C. Tobon-Gomez, L. Nace, A. Blum,
622 P. A. G. Teixeira, Automatic rib cage unfolding with CT cylindrical projection
623 reformat in polytraumatized patients for rib fracture detection and
624 characterization: Feasibility and clinical application, *Eur J Radiol*. 110 (2019)
625 121-127.
- 626 31. L. Jin, J. Yang, K. Kuang, B. Ni, Y. Gao, Y. Sun, P. Gao, W. Ma, M. Tan, H.
627 Kang, J. Chen, M. Li, Deep-learning-assisted detection and segmentation of rib
628 fractures from CT scans: Development and validation of FracNet, *EBioMedicine*.

- 629 62 (2020) 103106.
- 630 32. X.H. Meng, D.J. Wu, Z. Wang, X.L. Ma, X.M. Dong, A.E. Liu, L. Chen, A fully
631 automated rib fracture detection system on chest CT images and its impact on
632 radiologist performance, *Skeletal Radiol.* (2021) 1821-1828.
- 633 33. R. Lindsey, A. Daluiski, S. Chopra, A. Lachapelle, M. Mozer, S. Sicular, D.
634 Hanel, M. Gardner, A. Gupta, R. Hotchkiss, H. Potter, Deep neural network
635 improves fracture detection by clinicians. *Proc Natl Acad Sci U S A.* 115 (2018)
636 11591-11596.
- 637 34. E. Yahalomi, M. Chernofsky, M. Werman, Detection of Distal Radius Fractures
638 Trained by a Small Set of X-Ray Images and Faster R-CNN, *Intelligent*
639 *Computing-Proceedings of the Computing Conference.* (2019) 971-981.
- 640 35. Y.L. Thian, Y. Li, P. Jagmohan, D. Sia, V.E.Y. Chan, R.T. Tan, Convolutional
641 Neural Networks for Automated Fracture Detection and Localization on Wrist
642 Radiographs, *Radiol Artif Intell.* 1 (2019) e180001.
- 643 36. D.H. Kim, T. MacKinnon, Artificial intelligence in fracture detection: transfer
644 learning from deep convolutional neural networks, *Clin Radiol.* 73 (2018) 439-
645 445.
- 646 37. G. Kitamura, C.Y. Chung, B.E. Moore, Ankle Fracture Detection Utilizing a
647 Convolutional Neural Network Ensemble Implemented with a Small Sample, *De*
648 *Novo Training, and Multiview Incorporation,* *J Digit Imaging.* 32 (2019) 672-
649 677.
- 650 38. O. Ronneberger, P. Fischer, T. Brox, U-net: Convolutional networks for
651 biomedical image segmentation, *International Conference on Medical image*
652 *computing and computer-assisted intervention,* Springer (2015) 234–241.
- 653 39. J. Liu, G. Zhao, Y. Fei, M. Zhang, Y. Wang, Y. Yu, Align, attend and locate:
654 Chest x-ray diagnosis via contrast induced attention network with limited
655 supervision, *Proc IEEE Int Conf Comput Vis.* (2019) 10631-10640.
- 656 40. A.F. Tredgold, Variations of ribs in the primates, with especial reference to the
657 number of sternal ribs in man, *Journal of anatomy and physiology.* 31 (1897)
658 288.
- 659 41. M. Everingham, L.V. Gool, C.K.I. Williams, J. Winn, A. Zisserman, The pascal
660 visual object classes (VOC) challenge, *Int J Comput Vis.* 88 (2010) 303-338.
- 661 42. J. Lian, J. Liu, S. Zhang, K. Gao, X. Liu, D. Zhang, Y. Yu, A Structure-Aware
662 Relation Network for Thoracic Diseases Detection and Segmentation, *IEEE*
663 *transactions on medical imaging.* 2021.
- 664 43. R. Padilla, S. Netto, E. Silva, A Survey on Performance Metrics for Object-
665 Detection Algorithms, *international conference on systems, signals and image*
666 *processing (IWSSIP), IEEE.* (2020) 237-242.
- 667 44. S. Ren, K. He, R. Girshick, J. Sun, Faster R-CNN: towards real-time object
668 detection with region proposal networks, *IEEE transactions on pattern analysis*
669 *and machine intelligence.* 39 (2016) 1137-1149.
- 670 45. J. Pang, K. Chen, J. Shi, H. Feng, W. Ouyang, D. Lin, Libra R-CNN: Towards
671 balanced learning for object detection, *Proc IEEE Comput Soc Conf Comput Vis*
672 *Pattern Recognit.* (2019) 821-830.

-
- 673 46. H. Zhang, H. Chang, B. Ma, N. Wang, X. Chen, Dynamic R-CNN: Towards
674 High Quality Object Detection via Dynamic Training, European Conference on
675 Computer Vision. 2020.
- 676 47. Z. Cai, N. Vasconcelos, Cascade R-CNN: Delving into High Quality Object
677 Detection, Proc IEEE Comput Soc Conf Comput Vis Pattern Recognit. (2018)
678 6154-6162.
- 679 48. A. Bochkovskiy, C.Y. Wang, H.Y.M. Liao, YOLOv4: Optimal Speed and
680 Accuracy of Object Detection, 2020.
- 681